Lab on a Chip

PAPER

View Article Online
View Journal | View Issue



Cite this: *Lab Chip*, 2024, **24**, 5374

# An imaging scheme to study the flow dynamics of co-flow regimes in microfluidics: implications for nanoprecipitation†

Wali Inam, [a] Anton Vladyka, [c] Joanna W. Pylvänäinen, [d] Junel Solis, [d] Dado Tokic,[d] Pasi Kankaanpää[d] and Hongbo Zhang *[ab]

Co-flow microfluidics, in addition to its applications in droplet generation, has gained popularity for use with miscible solvent systems (continuous microfluidics). By leveraging the short diffusional distances in miniature devices, processes like nanomaterial synthesis can be precisely tailored for high-throughput production. In this context, the manipulation of flow regimes—from laminar to vortex formation, as well as the generation of turbulent and turbulent jet flows—plays a significant role in optimizing these processes. Therefore, a detailed understanding of fluid interactions within microchannels is crucial. Imaging with tracer particles is a commonly used approach to study fluid behavior. Alternatively, label-free imaging methodologies are rarely employed for studying fluid dynamics. In this pursuit, we present a new imaging-based scheme to explore fluid interactions in various co-flow regimes through optical flow analysis, specifically using Gaussian window mean squared error (MSE). By examining fluid flow characteristics such as flow intensities (caused by fluctuations) and the projected movement of fluid spots, we characterize slow vortexing and chaotic flow behaviors in co-flow regimes. Consequently, we use imaging data to illustrate the influence of co-flow regimes on particle synthesis. This new tool provides the scientific community with an innovative method to study fluid interactions, which can be further explored to develop a more effective understanding of fluid mixing and optimize fluid manipulation in microfluidic devices.

Received 6th August 2024,
Accepted 27th October 2024

DOI: 10.1039/d4lc00652f

rsc.li/loc



## Introduction

In the arena of recently developed state-of-the-art technologies,[1,2] microfluidics has emerged at the forefront of continuing advancements in diagnostics, nanomedicine and drug discovery.[3–5] The benefits offered by microfluidics and miniature devices, such as smaller-scale dimensions, larger surface area, quick heat dissipation and high diffusion rates, add versatility that distinguishes microfluidics from the conventional techniques for bulk processing.[6,7]

In the field of nanomaterials, microfluidics has shown tremendous growth as a platform for nanoparticle synthesis. Among many approaches to synthesize nanoparticles, such as self-assembly,[8] solvent displacement,[9] and ion exchange,[10] nanoprecipitation is the most widely explored technique in microfluidics.[11] In a typical nanoprecipitation, upon the controlled introduction of a polymer solution into a non-solvent, particles are formed through nucleation under supersaturated conditions, followed by diffusion-limited growth.[12,13] The process of nanoprecipitation is thus influenced by many factors, including the solvent system,[14,15] polymer properties,[16] mixing conditions[17] and device geometry.[18]

In microfluidics devices for particle synthesis, co-flow—comprising two coaxially aligned channels for propelling fluids in the same direction—is a simple and extensively used geometry.[19] By configuring the flow ratio (FR) of the co-axially propelled fluids, different flow regimes can be managed through alteration of the Reynolds number (ratio of inertial flow *vs.* viscous flow).[20] At one extreme (Re $<$ 2000), the fluid behavior is in the laminar regime, in which molecular diffusion serves as the main mechanism for fluid mixing. The minimum mixing time ($\mathcal{T}_{min}$) for the laminar stream is thus expressed as $\mathcal{T}_{min} \approx w_f^2/4D$ (where "$D$" is the diffusivity of the solvent, and "$w_f$" is the width of the focused stream).[13,21] Whereas at the other extreme, the flow adopts the turbulent regime (Re $>$ 2000) as inertial forces start to overcome the viscous effect of the fluids. However, before fully turbulent flow is developed, chaotic flow is observed as the laminar flows become unstable and transition to chaos. The flow

[a] *Pharmaceutical Sciences Laboratory, Faculty of Science and Engineering, Åbo Akademi University, Tykistökatu 6A, 20520 Turku, Finland. E-mail: hongbo.zhang@abo.fi*
[b] *Bioscience Centre, University of Turku and Åbo Akademi University, Turku, Finland*
[c] *Department of Physics and Astronomy, University of Turku, 20014 Turun yliopisto, Finland*
[d] *Turku Bioimaging, University of Turku and Åbo Akademi University, Turku, Finland*
† Electronic supplementary information (ESI) available. See DOI: https://doi.org/10.1039/d4lc00652f

instabilities caused in the fluid flow lead to the formation of vortices and other coherent complex structures.[22]

Studying the dynamics of chaotic or complex turbulent flow is a challenging proposition. In this regard, imaging techniques have been well explored, including velocimeter-based techniques such as micro particle imaging velocimetry (μPIV)[23] and laser doppler velocimeters.[24] These techniques are expensive to operate, often rely on the imaging of tracer particles/molecules, and lack the propensity to give accurate measurements in a continuous flow dynamics.[25] To eliminate the need for labeled particles and reduce instrumentation costs, an alternative approach could be developed based on optical image analysis to study fluid flow regimes in co-flow microfluidics. Therefore, there is a clear need to explore image analysis methods to understand fluid flow mechanisms in these microfluidic systems.

Therefore, we have developed an imaging scheme to study the interaction of fluids in co-flow through a high-speed digital microscopy and scheme for sequential image analysis involving: (1) drift correction (DC, rectify the vibrational influence from the environment); (2) a Gaussian window MSE algorithm function (for the detection and visualization of flow instabilities); (3) data extraction (data matrix); and (4) data analysis. Finally, nanoparticle synthesis was performed (model polymer) using the co-flow regime in microfluidics at different polymer concentrations (0.5 mg $mL^{-1}$ to 5 mg $mL^{-1}$). From our imaging data, we observed slow oscillatory vortexing at a slow outer flow rate ($Q_o$ = 166.7 μL $min^{-1}$) and consistent flow intensities in more chaotic flow regimes ($Q_o$ = 666.7 μL $min^{-1}$). Consequently, we illustrate the implications of the studied co-fluid regimes on particle size, particle size customization, and polydispersity. Therefore, we have laid out a systematic imaging scheme to study the interaction of fluids in a co-flow regime to understand fluid mixing and process optimization. Fig. 1 presents a systematic description of the methodology.

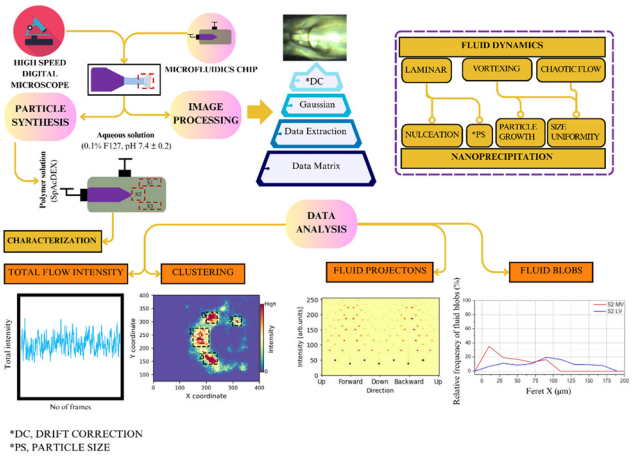


**Fig. 1** The imaging scheme used to study chaotic flow consisted of three steps: drift correction, Gaussian window MSE application, and data extraction by TrackMate. Our data analysis based on the data extracted using TrackMate was performed on total flow intensity (TFI), clustering of fluid spots based on an intensity-weighted density map, and fluid projection analysis based on the trajectory angle of the fluid spot and fluid blob analysis.

# Methods

### Microfluidics chip construction

Microfluidics chips were assembled with a narrow borosilicate glass capillary possessing an internal diameter of 580 μm (Sutter Instrument Co.) and a wider borosilicate glass capillary with an internal diameter of 1100 μm (Sutter Instrument Co.). The narrow glass capillary (580 μm) was first elongated with a puller (Model PN-31) to form a tapered end. The closed end of tapered capillary was gently rubbed with sandpaper to obtain an opening of approximately 130 μm. Thereafter, three segments of wider outer capillary were made with help of a glass cutter, and the tapered-end capillary (inner capillary) was inserted into the segmented outer capillary. The inner and outer capillary combo was placed on a glass slide (75 × 25 mm, J. Melvin freed brand) and a hypodermic needle (20 g Pk 12 SN-20) was fixed on the junction between the segment of the outer glass capillary. Metal connectors were inserted in the two open ends of the outer capillary. Lastly, devcon-5 minute epoxy was poured to seal the chip. The chip was left overnight to complete the process of sealing.

### Rheology of fluids

Prior to fluid flow imaging, rheology measurements of the fluids were performed to determine the fluid viscosity and fluid deformation to characterize Newtonian or non-Newtonian behaviour. In the current study, rheology experiments were performed using an organic polymer solution (SpAcDEX) and aqueous Poloxamer 407 solution in the inner and outer capillary of co-flow microfluidics device, respectively.

The rheological properties of the fluids were evaluated using a HAAKE™ MARS™ 40 advanced modular rheometer system (version 4.87.001, Thermo Scientific, Karlsruhe, Germany). The setup included a rotor plate (P35/Ti, 35 mm diameter) and a lower plate (TMP 35). The zero point was set at 0.485 mm, and the temperature was controlled at 23 °C. Prior to each measurement, the samples were sonicated and vortexed for 20 to 30 seconds. After a 60 second equilibration period, the measurements were conducted with a shear rate ramp ranging from 0.01 to 1000 $s^{-1}$ and lasting 350 seconds, with data being collected every 8 seconds. The HAAKE™ RheoWin job manager software recorded the measurements, and the data were analyzed using the HAAKE™ RheoWin data manager (version 4.87.001). Each sample was measured twice, and a third measurement was only performed if discrepancies were noted between the initial two runs.

### Setting up flow regimes

The microfluidics setup consisted of the co-flow device, two Harvard pumps (PHD 2000, Harvard Apparatus, USA) and a high-speed digital microscope (Meros). The connector leading to the inner tapered-end capillary and the one opening to the outer

capillary were connected to ethanol- and water-filled syringes fixed onto the pump, respectively. The high-speed digital microscope was used to image the flow. To generate different co-flow regimes, the inner flow ($Q_i$) was kept constant at 33.3 μL $min^{-1}$ and the outer flow ($Q_o$) was sequentially set to 166.7 μL $min^{-1}$, 333.3 μL $min^{-1}$, 666.7 μL $min^{-1}$, and 1666.7 μL $min^{-1}$. The flow regimes were designated as F1 ($Q_o$; 166.7 μL $min^{-1}$), F2 ($Q_o$; 333.3 μL $min^{-1}$), F3 ($Q_o$; 666.7 μL $min^{-1}$) and F4 ($Q_o$; 1666.7 μL $min^{-1}$). Control experiments were performed by capturing mono-flow with ethanol at 33.3 μL $min^{-1}$ in the inner capillary and water in the outer capillary at 166.7 μL $min^{-1}$, 333.3 μL $min^{-1}$, 666.7 μL $min^{-1}$ and 1666.7 μL $min^{-1}$.

### Fluid flow imaging

To image the flow behavior, the high-speed digital microscope (Meros) was set to the lowest magnification (0.5×) to obtain a better view of the microfluidics channels, and mitos flow control center (version 3.1.42) software was used to adjust the image quality and related settings, and to initiate the process of capturing videos. Videography was performed at 30 fps, restricted to 500 frames for a time length of 16 s. For flow regime F2, 1500 frames of video were captured until for a duration of 48 s to obtain a more stable flow. Video was recaptured if any discrepancy was found. Both the co-flow regimes and mono-flow (controls) were imaged the using same protocol.

### Drift correction and fluid flow analysis

Video encompassing 500 to 1500 stacked images of each flow was captured. To rectify motion resulting from the vibrations caused by pump operation, a drift correction was applied to the recorded video using NanoJ-Core.[26] Subsequently, the optic flow was estimated for the stack of images using the Gaussian Window MSE operation function in Fiji.[27]

The Gaussian window MSE method for optic flow detects motion by comparing pixel intensities between two consecutive images. A Gaussian window applies weighted smoothing over a local region, giving more importance to central pixels. The algorithm calculates the mean squared error (MSE) between pixel intensities in the two images and finds the displacement (motion vector) that minimizes this error within the Gaussian window. The magnitude of this displacement is then used to assign intensity values, creating an optic flow image that visualizes the motion between frames.

Based on this algorithm, we could track the fluid motion resulting from flow fluctuations or vortex formation leading to formation of vortices in different flow regimes. Image processing of both co-flow regimes and mono-flow (controls) were done using the same protocol.

### Data extraction and image analysis

The data extraction after the application of the Gaussian window MSE function was performed using TrackMate.[28] The label image detector identifies and tags different fluid spots and enumerates parameters for each spot, such as flow intensity, flow trajectory ($\theta$), and area, along with shape indicators such as ellipse, perimeter, circularity, and solidity. Thus, data was collected for each image using label image detection. Therefore, a complex data matrix was generated, which was later used for in-depth analysis by examining the total intensity as a function of time, flow distribution in clusters and shape analysis of fluid blobs.

### Fluid blob analysis

Fluid blobs are single fluid spots or groups of fluid spots that represent a cohesive region of fluid that exhibits irregular motion and has a defined boundary and geometry. The shape transformation and stretching of fluid bobs was studied to determine the flow pattern, mixing regions and impact of the stresses induced by the environment. Fluid blobs were marked by performing thresholding (50–250) using Fiji. After thresholding, Feret*X* (length of the pattern in the *x* dimension) and Feret*Y* (length of the pattern in the *y* dimension) were measured to perform shape analysis.

### Nanoparticle synthesis

Four polymer solutions were prepared by dissolving 1 mg, 2 mg, 5 mg, and 10 mg of spermine-modified acetylated dextran (SpAcDEX) in 2 mL of ethanol to obtain final concentrations of 0.5 mg $mL^{-1}$, 1 mg $mL^{-1}$, 2.5 mg $mL^{-1}$, and 5 mg $mL^{-1}$. Each concentration was treated in the following manner.

Polymer solution and non-solvent 0.1% Poloxamer 407 (Pluronic F127, mol. weight 12 500 Daltons, pH 7.4 ± 0.2) solution were infused in the inner and outer capillary of the co-flow microfluidics, respectively, with the aid of Harvard Apparatus (PHD 2000, USA). The flow rate of the polymer solution was at kept at 33.3 μL $min^{-1}$, whereas flow rate of the aqueous solution (0.1% F127, pH 7.4 ± 0.2) was set to 166.7 μL $min^{-1}$, 333.3 μL $min^{-1}$, 666.7 μL $min^{-1}$ and 1666.7 μL $min^{-1}$. The produced particles were collected in a glass vial and centrifuged (13 000 rpm) for 10 minutes to collect white pellets. The particles were washed once with distilled water (pH 8) by sonication and vortex mixing, and then centrifuged. Each synthesis experiment was performed in triplicate.

### Dynamic light scattering (DLS)

Colloidal parameters such as hydrodynamic particle diameter and polydispersity index (PDI) were characterized *via* the DLS technique using a Zetasizer Nano ZS instrument (Malvern Panalytical Ltd., Malvern, UK). Sample preparation for all samples was performed in an identical manner; a dilution of the nanoparticles collected from the co-flow microfluidics device was prepared by dispersing 200 μL of the nanoparticle dispersion in 10 mL of distilled water. The diluted nanoparticle suspensions (1 mL) were transferred to disposable cuvettes (Malvern Panalytical Ltd.) and placed in the sample holder of the instrument to perform size measurements. Zetasizer measurements were performed in general purpose mode. Measurement runs were set to automatic mode with maximum allowed runs of 100, while repeated cycles of runs for each

 

measurement were fixed to 3; we comprehensively discuss the reporting of DLS in our latest review.[29]

To measure the electrophoretic mobility, nanoparticle dilutions were prepared in 25 mM HEPES buffer (pH 7.2 ± 0.2), which was filled carefully into the folded capillary cells (DTS1070) with the help of a dropper to avoid bubble entrapment. The electrophoretic mobility cell was placed in the sample holder and three sets of measurements were recorded. Zeta potential values were calculated from the electrophoretic mobility values using the Henry equation.[30,31]

# Results

Ethanol and water were flown through the tapered-end inner capillary and wider outer capillary, respectively, in a co-flow microfluidics device. Four flow regimes were generated by setting the outer flow rate ($Q_o$) to 166.7 μL min$^{-1}$ (F1), 333.3 μL min$^{-1}$ (F2), 666.7 μL min$^{-1}$ (F3) and 1666.7 μL min$^{-1}$ (F4) respectively, while keeping the inner flow rate ($Q_i$) constant at 33.3 μL min$^{-1}$. All flow regimes were produced with Re numbers ranging from 27 to 273. The detailed parameters of the co-flows generated are given in Table 1.

### Image analysis scheme

Video of each flow regime was recorded as described in the methodology section, and the imaging scheme was applied (drift correction (DC) > Gaussian window MSE > TrackMate). The Gaussian Window MSE used for optic flow visualization compares pixel intensities between two sequential images for tracking motion. The algorithm computes the mean squared error (MSE) between pixel intensities in both images and determines the shift (motion vector). The magnitude of this displacement is then used to assign intensity values, resulting in an optic flow image that captures the movement between the frames. Data extraction was performed using TrackMate and the following important parameters were studied further: (i) fluid spots, single data points that represent groups of pixels (sharing closely associated magnitude and vector quantities) in close vicinity. ii) Fluid blobs, which are single fluid spots or groups of fluid spots representing a cohesive region of fluid that exhibits irregular motion, and has a defined boundary and geometry. iii) Flow intensity, which refers to the magnitude of the intensity of the fluid exhibiting fluctuations due to non-laminar flow, which was graded on the grayscale values of the pixels (0–255). ii) Flow trajectory, which is measurement of the angle at which each fluid spot is headed in a given space and time. The direction values were graded and adjusted for the grayscale values (0 to 255).

**Table 1** Flow regime parameters, inner flow ratio (ethanol), outer fluid ratio (water), Reynolds number (Re)

| Flow regime | Inner FR | Outer FR | FR | Re |
|---|---|---|---|---|
| F1 | 33.3 μL min$^{-1}$ | 166.7 μL min$^{-1}$ | 0.2 | 27 |
| F2 | 33.3 μL min$^{-1}$ | 333.3 μL min$^{-1}$ | 0.1 | 54 |
| F3 | 33.3 μL min$^{-1}$ | 666.7 μL min$^{-1}$ | 0.05 | 108 |
| F4 | 33.3 μL min$^{-1}$ | 1666.7 μL min$^{-1}$ | 0.02 | 273 |

Inner FR (ethanol), outer FR (water), Re (Reynolds number).

### Flow regime imaging analysis

High-speed digital microscopy imaging showed that upon increasing $Q_o$ from 166.7 μL min$^{-1}$ to 1666.7 μL min$^{-1}$, the length of the laminar stream increased. At the highest $Q_o$ of 1666.7 μL min$^{-1}$ (F4), the flow becomes completely laminar, with the ethanol stream flowing in middle of the outer capillary (Fig. 2m). However, the laminar ethanol stream expands into a conical tail in the F1, F2 and F3 flow regimes (Fig. 2d, g and j). Some vortices were observed in the conical trail region, which were further analysed using the Gaussian window MSE function.

Images of all four flow regimes (F1. F2, F3 and F4) and the controls (mono-flow setup, ethanol $Q_i$ (33.3 μL min$^{-1}$, water $Q_o$ 166.7 μL min$^{-1}$) were computed based on the average intensity of the fluid spots (Fig. 2). Flow intensity is illustrated by the white spots against the black background, whereas the brightness of spot correlates with the magnitude of flow intensity. In the F1 flow regime, weak flow intensity was observed around a semi-circular path with a diminished core (Fig. 2e), indicating the formation of vortices.

Similarly, flow intensity in the F2 flow regime is also detected around a semi-circular path (Fig. 2h), indicating the formation of vortices. However, the relatively high flow rate intensity observed indicated stronger interaction between the fluids. The computed image for the F3 regime showed a claw-

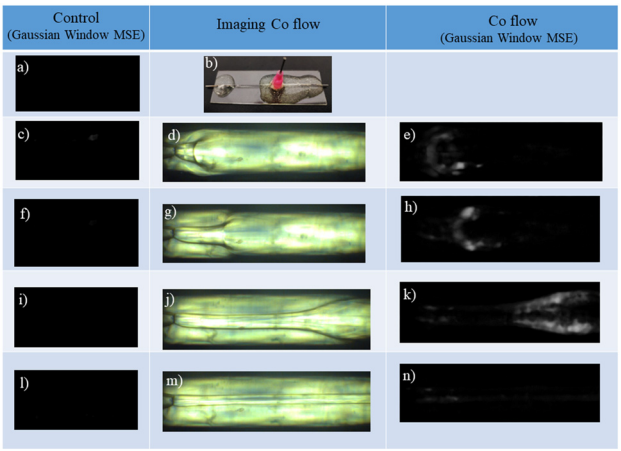


**Fig. 2** Gaussian-transformed images of the controls: a) only ethanol flowing through the inner capillary, or only water flowing through the outer capillary at c) $Q_o$ 166.7 μL min$^{-1}$, f) $Q_o$ 333.3 μL min$^{-1}$, i) $Q_o$ 666.7 μL min$^{-1}$ and l) $Q_o$ 1666.7 μL min$^{-1}$. b) Photograph of the co-flow device. Digital high-speed microscopy imaging of the four co-flow regimes (water in the inner capillary and ethanol in the outer capillary): d) F1 flow regime, g) F2 flow regime, j) F3 flow regime and m) F4 flow regime. Images computed based on the average flow intensity from all fluid spots over the period of time for all co-flow regimes after application of Gaussian window MSE: e) F1 flow regime, h) F2 flow regime, k) F3 flow regime and n) F4 flow regime. The bright spots indicate intensity generated by the fluctuating flow with inner and outer fluid interaction during co-flow.

shaped flow intensity spread over a much larger area (500 μm) at the interface of the outer and inner fluid (Fig. 2k). The fact that no intensity was observed in the F4 flow regime (Fig. 2n) illustrates that once complete laminar flow is achieved, fluid interaction and flow fluctuations are minimized. Similarly, no flow intensity was observed in the controls (Fig. 2). Hence, these results verify that flow intensity is only observed due to flow fluctuation and the interaction of fluids.

### Analysing flow in clusters

To analyse the distribution of flow intensity around the area of fluctuating flow, we mapped fluid spots in an intensity-weighted density plot. The data showed that the fluid spots form clusters with dense cores corresponding to a high number of fluid spots (Fig. 3a). These clusters are likely the contact points of high chaos as the two meet when vortices are produced. For example, clusters 0 and 2 in the F1 flow regime and clusters 1 and 4 in the F2 flow regime are situated in close proximity to the outer fluid and show high density as compared to the other clusters in the respective flow regimes (Fig. 2a and b). In the F3 flow regime, clusters 0 and 1 have significant size and density, corresponding to a high degree of chaos (Fig. 3c) Thus, analysis of the fluid clusters gives information about the distribution of flow intensity around vortices as well as points of high chaos.

### Total intensity as a function of time

The fluctuations and instabilities caused by the interaction of ethanol as the inner fluid and water as the outer fluid are altered with changes in $Q_o$. Therefore, the total intensity was studied as a function of time. The results showed that at the lowest flow rate of $Q_o$ = 166.7 μL min$^{-1}$ (F1 flow regime), the total intensity exhibits oscillations, forming three zones. Each zone comprised five to six peaks. The first set of oscillations was observed between $t$ = 2.5 s and $t$ = 5.5 s, corresponding to frames 81–171. The second set of oscillations was found between $t$ = 8 s and $t$ = 11.5 s corresponding to frames 261–271. The third zone extended from $t$ = 13 s to $t$ = 16 s (corresponding to frame numbers 405 to 494) (Fig. 4a). To investigate the oscillatory nature of the F1 flow regime, we performed Fourier analysis on the total intensity data of each cluster. Interestingly, we found that cluster 1 exhibited first, second and third harmonic frequencies of 2.7 Hz, 5.4 Hz and 8.1 Hz, respectively (ESI† Fig. S1). Cluster 2 oscillated at the first and second harmonic frequencies (2.7 Hz and 5.4 Hz), and cluster 3 exhibited the first and third harmonic frequencies (Fig. S1, ESI†). This harmonic fluid flow intensity indicates rhythmic interaction between the two miscible fluids and displays the generation of slow vortexing behaviour in the F1 flow regime that could influence fluid mixing.

Upon increasing the $Q_o$ to 333.3 μL min$^{-1}$ (F2 flow regime), the total oscillation intensity decreased, and two zones of high intensity were observed. Zone 1 extended between frames 440 and 900 and persisted for 20 s, while the shorter zone 2 existed between frames 1120 and 1500 and lasted for 16 s, (Fig. 4b). The total intensity values were significantly higher than in the F1 flow regime (correlating well with the cluster analysis) due to the rapid rate of interaction between the two miscible fluids. This fast fluid flow fluctuation led to fast vortexing.

The total intensity data showed that when $Q_o$ is increased two-fold to 666.7 μL min$^{-1}$, the rate and strength of interaction further increase, generating continuous and high flow intensity. The total intensity values were significantly higher than in the F2 and F1 flow regimes, showing vigorous flow fluctuations (Fig. 4c).

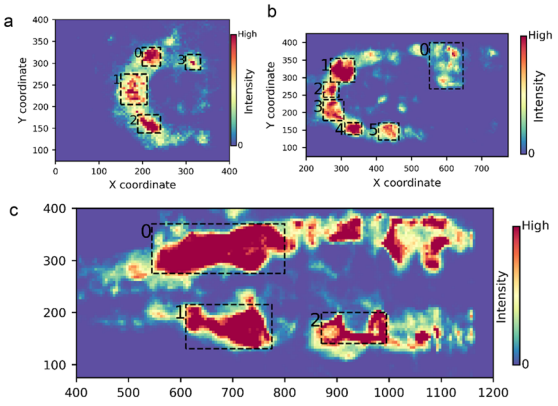


Fig. 3 Intensity-weighted density map. Co-flow regimes with ethanol as the inner flow and water as the outer flow: a) F1 flow regime, b) F2 flow regime and c) F3 flow regime. Clusters shown as dense spots are marked with numbers. Colour mapping indicates the density of the spots estimated based on the flow intensity. The highest density corresponds to the red areas.

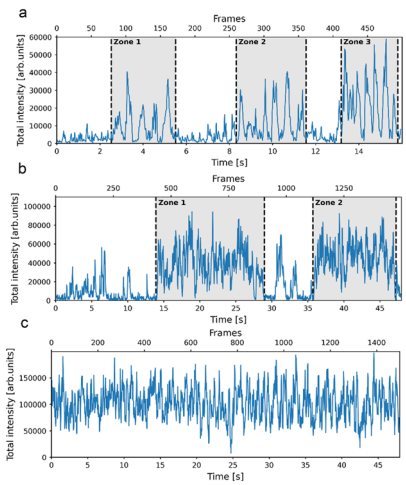


Fig. 4 Total intensity as a function of time. Total intensity is calculated by summing the mean intensities of all the fluid spots for a unit of time. Co-flow regimes with ethanol as the inner flow and water as the outer flow: a) F1 flow regime, b) F2 flow regime and c) F3 flow regime. Oscillating zones are marked in gray.

### Fluid projection analysis

Analysis of the movement and trajectory of fluids is critical for understanding chaos in a system.[32] Rather than the commonly employed traceable particles used to predict and track fluid movement,[33,34] here, we have used the angle of trajectory angle ($\theta$) data of the fluid spots derived with Gaussian window MSE to estimate the movement of the fluid in each flow regime. The angle of trajectory ($\theta$) for each fluid was estimated per unit time (scaled 0–255).

Rapidly changing flow trajectory is one of the characteristic features of a chaotic or turbulent system.[35] Therefore, to analyse the chaos in the flow regimes, we studied the intensity weighted direction *vs.* intensity heat map (Fig. 5). For the sake of simplicity, the directions based on trajectory angle directions were classified as upward, downward, backward and forward. Based on the heat map analysis, the fluid spots in the F3 flow regime showed the broadest distribution of fluid spots along the direction axis, with the fluid spots showing a bimodal distribution in the forward and backward direction. The F4 flow regime, in contrast, was thinly populated with fluid spots narrowly distributed along the distance axis. The fluid spots in the F2 flow regime showed a broader distribution along the direction axis compared to the F1 flow regime.

### Fluid blob analysis

The coherent structures generated during fluid mixing elucidated by tracer particles are characteristic features of flow regimes.[36] The Gaussian Window MSE operation function, in addition to tracking fluid motion through the intensity and angle of trajectory, also computes the shape and dimensions of force fields termed as fluid blobs (Fig. S2, ESI†). By studying how the dimensions of the fluid blobs change in different flow regimes, we aim to understand the fluid flow pattern. For the sake of simplicity, we focused on three regions, the SP1 region parallel and close to the top wall of the outer capillary, the S2 region in the middle and close to the tapered-end capillary and the S3 area close and parallel to the lower wall of the outer capillary (Fig. 6).

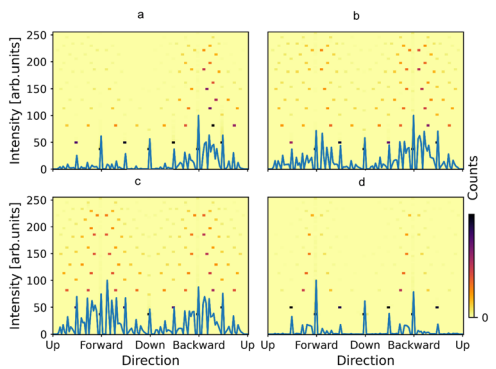


Fig. 5 Intensity-weighted heap map of the fluid spots plotted as *a* direction (*x*-axis) *vs.* intensity (*y*-axis) plot for the co-flow regimes with ethanol as the inner flow and water as the outer flow: a) F1 flow regime, b) F2 flow regime, c) F3 flow regime and d) F4 flow regime.

### Analysis and comparison of S1 region

We compared the movement of fluids in the S1 region of the F1, F2 and F3 flow regimes. A comparison of relative percentage frequency of fluid blob lengths along the *x* axis as measured by Feret*X* shows that fluid blobs in the F1 and F2 flow regimes mostly stretch 10 μm horizontally (~40%) (Fig. 6). In comparison, the fluid blobs in the F3 flow regime extend from 200 to 400 μm. The fluid blobs in the F3 flow regime have longer horizontal extension in comparison to the other flow regimes.

Feret*Y* was studied to evaluate the vertical extension of the fluid blobs. The vertical extension of the fluid blobs (Feret*Y*) ranged from 10 to 30 μm (56%, F1 flow regime), 30 to 70 μm (76%, F2 flow regime) and 70 to 130 μm (66%, F3 flow regime) (Fig. 6). The Feret*Y* analysis shows that the vertical extension of the fluid blobs increases as the flow rate is increased from 33.3 μL $min^{-1}$ to 1666.7 μL $min^{-1}$ as the flow regime transitions from F1 to F2.

The overall comparison of the fluid blob extension in the *x* and *y* dimensions in the SP1 region of the F1, F3 and F2 flow regimes shows that fluid blobs occupying the S1 region in the F1 regime are small and spherical in shape (with approximately equal *x* and *y* extensions). In the F2 regime,

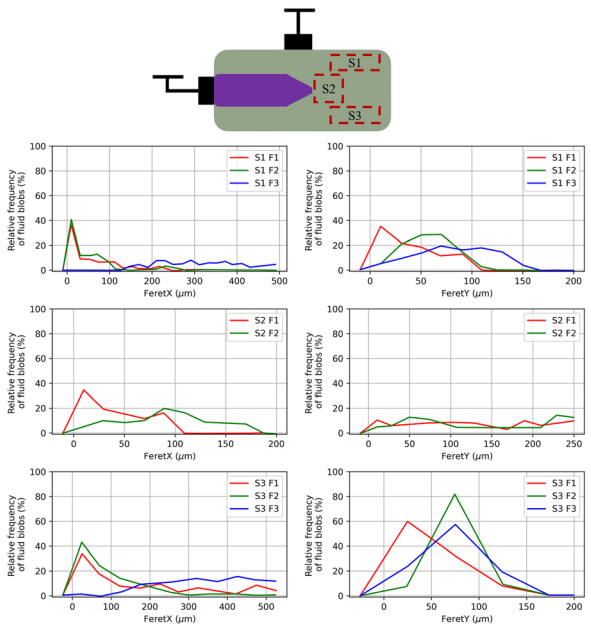


Fig. 6 Line graphs illustrating the percentage relative frequency of the S1 and S3 region fluid blobs in the co-flow regimes: F1, F2, and F3. The co-flow regimes are generated with ethanol as the inner flow and water as the outer flow. The extensions of the fluid blobs plotted along *x* and *y* axes were measured using Feret*X* and Feret*Y*, respectively. The parameters Feret*X* and Feret*Y* were measured by applying thresholding (50–255) in Fiji.

the fluid blobs are elliptical in shape and oriented vertically. In contrast, the fluid blobs are large, elongated and stretched horizontally in the F3 regime. The elliptical fluid blobs and extended horizontal structures indicate enhanced stretching of the material lines along the length of the capillary.

### Analysis and comparison of the SP2 region

Comparison of the SP2 region shows that the F1 regime has two populations of fluid blobs horizontally extending to Feret*X* lengths of 10 μm (35%) and 90 μm (16%), (Fig. 6). In the F3 regime, the fluid blobs have a Feret*X* length of 90 μm (20%, Fig. 6).

Analysis of the vertical dimensions of the fluid blobs shows no significant difference between the F1 and F3 flow regimes. In the SP2 region, the fluid blobs appear small and spherical with no significant extension in the horizontal or vertical direction.

### Analysis and comparison of the S3 region

The analysis of the S3 region of the F1 and F2 regimes shows smaller fluid blobs (sub-100 μm) in both regimes, whereas fluid blobs with sizes greater than 200 nm are found in the S3 region of F1 regime (Fig. 6). In comparison, the fluid blobs in the F2 and F3 flow regimes compared across vertical extension have a Feret*Y* value of 75 μm (83% and 57% respectively) (Fig. 6). Based on the comparison of the Feret*X* and Feret*Y* analyses, the fluid blobs in the F1 regimen are smaller and exhibit a spherical shape.

In the F2 flow regime, the fluid blobs extend vertically, forming an elliptical shape. In the F3 flow regime, the fluid blobs are oriented horizontally, parallel to the length of the outer capillary wall (Fig. 6).

### Implications of co-flow regimes on nanoprecipitation

**Characterizing fluid rheology.** Fluid rheology significantly influences fluid flow behaviour, especially in the confined space of miniature channels. The change in viscosity in relation to the rate of shear is an important aspect of fluid rheology, which determines whether a fluid has Newtonian or non-Newtonian characteristics. To determine the rheological nature of the fluids (SpAcDEX and Poloxamer 407 solution) used in our experimental step, we used a HAAKE™ MARS™ 40 advanced modular rheometer system (version 4.87.001, Thermo Scientific, Karlsruhe, Germany) with a cone-plate geometry (35 mm) at 23 °C. The inner solution of SpAcDEX (0.5 mg $mL^{-1}$, 1 mg $mL^{-1}$, 1 mg $mL^{-1}$, 2.5 mg $mL^{-1}$ and 5 mg $mL^{-1}$) and outer solution of 0.1% Poloxamer 407 (pH 7.4 ± 0.2) showed relatively constant viscosity over shear rates ranging from 10 to 1000 1/s, which also shows that the polymer (SpAcDEX) and surfactant (Poloxamer) do not alter the rheological properties of the solvents. Thus, the fluid behaviour studied by imaging data could be correlated and compared to illustrate nanoprecipitation (Fig. 7).

**Microfluidics-assisted SpAcDEX particle synthesis.** To understand the implication of the imaging data analysis,

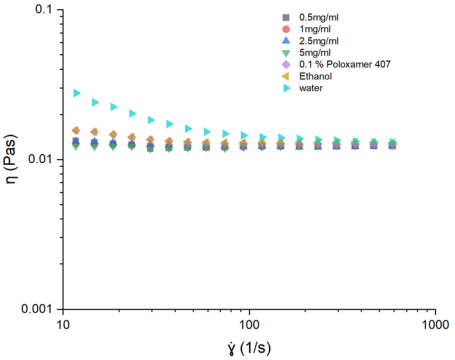


**Fig. 7** Fluid rheology characterized using a HAAKE™ MARS™ 40 advanced modular rheometer system (version 4.87.001, Thermo Scientific, Karlsruhe, Germany). A viscosity ($\eta$, Pac) *vs.* shear rate ($\dot{\gamma}$, 1/s) scatter graph was plotted for the inner solution of SpAcDEX in ethanol (0.5 g $mL^{-1}$, 1 mg $mL^{-1}$, 2.5 g $mL^{-1}$ and 5 mg $mL^{-1}$) and outer solution 0.1% poloxamer 407 polymer, while ethanol and water were used for comparison.

SpAcDEX particles were synthesized using the co-flow microfluidics device. The polymer solution was flown through the inner tapered-end capillary, and 0.1% Poloxamer 407 solution (pH 7.4 ± 0.2) was infused directly into the outer capillary. Particles were synthesized using the co-flow regimes F1, F2, F3 and F4 described earlier and polymer concentrations ranging from 0.5 mg $mL^{-1}$ to 5 mg $mL^{-1}$. The hydrodynamic particle diameters of the produced nanoparticles were characterized using dynamic light scattering, and the electrokinetic stability of the particles was studied by measuring their electrophoretic mobility and calculating of their zeta potential using a Zetasizer Nano ZS (Malvern Panalytical Ltd.).

**Impact of co flow regime on the particle size.** The hydrodynamic diameter of the nanoparticles studied by DLS showed a decline in particle size with increasing $Q_o$ (Fig. 8b). This trend in particle size was consistent across polymer concentrations of 0.5 mg $mL^{-1}$ to 2.5 mg $mL^{-1}$, (Fig. S4, ESI†). DLS characterization of particles synthesized at concentrations of 0.5 mg $mL^{-1}$, 1 mg $mL^{-1}$ and 2.5 mg $mL^{-1}$ showed respective hydrodynamic particle diameters of 210 ± 20 nm, 220 ± 20 nm, 260 ± 10 nm at the lowest $Q_o$ 166.7 μl $min^{-1}$ (F1 flow regime), whereas the hydrodynamic particle diameter was reduced to 153 ± 14 nm, 180 ± 10 nm, and 192 ± 5 nm at concentrations 0.5 mg $mL^{-1}$, 1 mg $mL^{-1}$ and 2.5 mg $mL^{-1}$, respectively, at the highest $Q_o$ of 1666.7 μL $min^{-1}$ (F4 flow regime) (Fig. 8b). The results show that the F4 laminar flow regime favours the synthesis of small particles.

**Impact of co flow regime on particle size customization.** Next, we were interested in examining the particle size customization potential of each flow regime. To do so, we studied the increase in the hydrodynamic particle diameter as the polymer concentration was raised to the next-highest concentration. The increase in the hydrodynamic particle diameter of the SpAcDEX particles was studied between concentrations of 1 mg to 0.5 mg (Con 1–0.5), 2.5 mg to 1 mg (Con 2.5–1), 5 mg to 2.5 mg (Con 5–2.5), and 5 mg to 0.5 mg

 

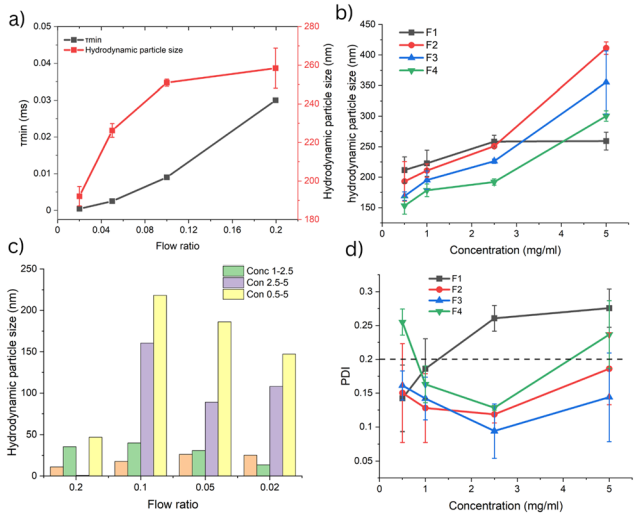


**Fig. 8** a) Hydrodynamic particle diameter (HD) and minimum mixing time ($\mathcal{T}_{min}$) plotted against flow ratio. b) Hydrodynamic particle size plotted against polymer concentration for the four flow regimes. c) The size customization of the SpAcDEX particles was studied by the measuring difference in particle size between the lower and next-highest concentration for each flow regime for polymer concentrations of 0.5 mg mL$^{-1}$ to 5 mg mL$^{-1}$. Conc 1–0.5, Con 2.5–5, and Con 5–2.5 represent the increment in particle size as the concentration is increased from 0.5 to 1 mg, 1 mg to 2.5 mg, and 2.5 mg to 5 mg, respectively for the flow ratios (FR) 0.2 (F1), 0.1 (F2), 0.05 (F3), and 0.02 (F4). d) Polydispersity index (PDI) of the particles plotted against polymer concentration (0.5 mg mL$^{-1}$ to 5 mg mL$^{-1}$) for all flow regimes.

(Con 5–0.5). Our analysis showed that for the concertation range 5–0.5 mg (Con 5–0.5), highest increase in hydrodynamic particle diameter of 218 ± 22 nm and 186 ± 44 nm was shown by the F2 (FR 0.1) and F3 (FR 0.05) flow regimes (Fig. 8c). Whereas an increment of 147 ± 5 nm and 47 ± 6 nm was exhibited by the F4 (FR 0.02) and F1 (FR 0.1) flow regimes, respectively (Fig. 8c). Thus our result suggests that F2 and F3 flow regimes provide more flexible control over the particle size, which correlates well with the polymer concentration, allowing more room for particle size customization.

**Impact of co flow regime on particle size uniformity.** The polydispersity index (PDI) is an important parameter and an indicator of particle size uniformity.[37] To understand the impact of the co-flow regimes on the uniformity of the SpAcDEX particles, we studied the polydispersity (PDI) of the particles produced by different flow regimes using a Zetasizer Nano ZS. It is noteworthy that there is no clear cut off value of PDI that marks particle size uniformity and monodisperse formulation synthesis. However, it is generally agreed that the lower the PDI values, the better the uniformity and the less polydisperse the formulation.[29]

The results show that the polydispersity of the particles is highly influenced by the $Q_o$, flow regime adopted and concentration of polymer. Therefore, optimum conditions are required to obtain uniformity in the particle size. When comparing PDI values between different polymer concentrations across different flow regimes, it was found that F2 and F3 flow regimes exhibited the lowest PDI values of 0.118 and 0.094 at a 2.5 mg mL$^{-1}$ concentration, respectively (Fig. 8d). In comparison, the F1 and F4 regimes showed high PDI values, indicating high polydispersity (Fig. 8d). Therefore in addition to more flexible particle size growth F2 and F3 flow regime also favour uniform particle synthesis.

## Discussion

To explore the dynamics of fluid flow in co-flow microfluidics, four flow regimes were generated by varying $Q_o$ from 166.7 to 1666.7 μL min$^{-1}$ (FR 0.2–0.01) in the low Reynolds number (27–273) range. After capturing each flow regime using high-speed digital microscopy, an image processing scheme was followed to compute and study the fluid flow motion caused due to inertial effects caused by interaction of two fluids. After rectifying the noise from the vibrational effects with drift correction, Gaussian Window MSE was applied and important parameters were extracted, such as fluid flow intensity, angle of projection, and distribution of fluid spots based on clustering, and the morphology of the fluid blobs was analysed to decipher the dynamics of each flow regime. Next, SpAcDEX particle synthesis was examined using the co-flow regimes in terms of hydrodynamic diameter, particle size customization and polydispersity.

The imaging data suggests that in the F1 flow regime (FR 0.2, $Q_o$ 166.7 μL min$^{-1}$) the detected flow intensity exhibits oscillation, (see Fig. 4a). The presence of oscillatory intensity (three oscillating zones) suggests slow interaction between the inner and outer fluids. Further, images computed based on the average flow intensities indicate that interaction occurs around a semi-circular path (Fig. 2e), suggesting the formation of vortices. Interestingly, the harmonic frequencies originating from clusters 1, 2 and 3 indicate that vortices are formed in a rhythmic fashion (see Fig. S2, ESI†). Analysing fluid projection using the angle of trajectory shows the dominance of back flow (Fig. 5a), which results in slower forward propulsion. Therefore, slow vortexing and high back flow would lead to accumulation of polymer precipitates resulting in larger and non uniform particle size (Fig. 8b and d).

With increasing $Q_o$ to 333.3 μL min$^{-1}$ (F2 flow regime), inner fluid extends as small laminar stream and immediately disturpting into a fluctuating flow. The total flow intensity studied as a function of time shows high intensity flow with fewer oscillations (two oscillating zones) (see Fig. 4b). Like in the F1 flow regime, flow intensity was detected around a semi-circular path, showing the formation of vortices. The randomization of fluid movement around a semi-circular path is depicted by the broad distribution of fluid spots in both the forward and backward direction (Fig. 5b). Based on the flow intensity and fluid projection analysis, the vertices formed in the F2 flow regime lead to more chaotic movement of fluid. In the F2 flow regime, the laminar stream promoting fluid mixing by diffusion ($\tau_{min}$ 0.009, Fig. 8a) is supplemented by the additional mixing by chaotic vortexing that forms smaller particles (Fig. 8b) with lower polydispersity (Fig. 8d)

and improved particle size customization compared to the F1 flow regime (Fig. 8c).

Upon increasing $Q_o$ to 666.7 μL min$^{-1}$ (F3 flow regime), the laminar flow extends further, and at the far end, flow fluctuations are observed, resulting in high flow intensity (Fig. 4c). The total intensity is detected to be produced continuously over time spread over a large distance. In addition, projection analysis shows an even broader distribution of fluid movement, indicating the generation of higher chaos. Further, the flow intensity is distributed more uniformly near the tapered-end inner capillary. Fluid blob analysis of the F3 flow regime shows that the force fields generated are large, elongated and stretched horizontally, indicating enhanced stretching of the material lines along the length of the capillary near the walls of outer capillary (Fig. 6). Therefore, in the F3 flow regime, diffusion-based mixing by the laminar stream ($\tau_{min}$ 0.0025, Fig. 8a) is further supplemented by chaotic-flow-based fluid mixing, leading to a further decrease in hydrodynamic particle size (Fig. 8b), lower polydispersity (Fig. 8d), a narrower particle size distribution (Fig. S3, see ESI†) and significant particle size customization (Fig. 8c).

Complete laminar flow was achieved at $Q_o$ 1666.7 μL min$^{-1}$ (F4 flow regime) with no flow fluctuation. Here, nanoprecipitation is caused by mixing assisted by only molecular diffusion across laminar flow ($\tau_{min}$ $4.2 \times 10^{-4}$, Fig. 8a). Due to instance nucleation, under the fast laminar flow, the particle size is further reduced (Fig. 8b), but at the expense of lack of monodispersity (high PDI, Fig. 8d). With laminar flow, the particle size customization is also reduced (Fig. 8c).

According to the LaMer mechanism,[38] nucleation and particle growth are two key components of nanoprecipitation. The formation nuclei begins in an instantaneous outburst from supersaturation; the following drop in concentration halts nucleation and the molecular diffusion of monomeric molecules promotes the growth of particles. Molecular diffusion in the laminar flow is a slow process. While vortexing or turbulent flow is known to greatly enhance mixing through folding, stretching and re-folding mechanisms.[39,40]

Hence, based on the above discussion, we conclude that the F2 and F3 flow regimes provide the most optimum conditions for nanoprecipitation. First, nucleation through the diffusion-based mixing of the fluid constituents across the laminar stream is achieved, while consequent exposure to vortexing or chaotic flow aids in providing homogeneity, smaller particle size and particles size customization by controlling nucleation and growth to assist the nanoprecipitation-based particle synthesis.

The imaging scheme presented in this study to examine flow fluctuation and unstable or chaotic flows allows characterization of different co-flow regimes; however, this methods is sensitive to noise, which may result from measurement or environmental factors. This effect can be minimized by applying drift correction. Due to the lack of labelling and limitation of the algorithm, complex flow structures cannot be accurately tracked. Taking these limitations into account, this imaging scheme could be combined with other techniques, such as micro-particle image velocimetry (μPIV), to help develop a more comprehensive understanding of fluid behavior in microfluidic systems.

## Conclusion

In this study, we have presented an imaging-based scheme to investigate the dynamics of co-flow regimes (F1, F2, F3 and F4) through examination of fluid flow intensities, fluid movement and fluid blob analysis. Based on our imaging scheme, we characterized slow oscillatory motion (vortices) and chaotic vortices/flow in co-flow microfluidics through analysis of fluid flow intensity, flow tracjectory, and flow distribution (cluster analysis). We then used the imaging data to explain the impact of each flow regime on nanoprecipitation-based particle synthesis. We showed that the vortices or chaotic flow generated in the F2 and F3 flow regimes greatly aid in particle size reduction, reduce polydispersity and provide flexible particle size customization.

Our imaging-based scheme is cost-effective and can be easily exploited to explore different unstable or vigorous fluid flows in miniature devices. Thereby, it can be used to improve the understanding of fluid flow dynamics, manipulation and process optimization, to foster automation in miniature devices.

## Data availability

Data supporting finding of this study are openly available in a public repository **https://zenodo.org/** *via* link **https://doi.org/10.5281/zenodo.13220903**.

## Author contributions

W. I. was involved in the conceptualization, investigation, methodology, and writing original draft. A. V. did data curation and formal analysis. JP, JS, DT, and PK aided in developing the methodology and software. HZ was involved in supervision, funding acquisition, review and correction.

## Conflicts of interest

There are no conflicts to declare.

## Acknowledgements

We acknowledge support and guidance provided in image analysis by the Turku Bioimaging Image Data Team at Åbo Akademi University and University of Turku. This work was supported by the Research Fellow (Grant No. 353146), Project (347897), Solution for Health Profile (336355), and InFLAMES Flagship (337531) grants from Academy of Finland. Biocenter Finland Bioinformatics and Drug Discovery and Chemical Biology networks, CSC IT Center for Science, Joe, Pentti and Tor Borg Memorial Fund, S. J. foundation are acknowledged.

## References


1 N. Baig, I. Kammakakam, W. Falath and I. Kammakakam, *Mater. Adv.*, 2021, **2**, 1821–1871.
2 J. Ge, B. Ding, S. Hou, M. Luo, D. Nam, H. Duan, H. Gao, Y. C. Lam and H. Li, *Nat. Commun.*, 2021, **12**, 1–8.
3 M. M. Islam, A. Loewen and P. B. Allen, *Sci. Rep.*, 2018, **8**, 1–11.
4 S. Abalde-Cela, P. Taladriz-Blanco, M. G. de Oliveira and C. Abell, *Sci. Rep.*, 2018, **8**, 2440.
5 A. Fabozzi, F. Della Sala, M. Di Gennaro, N. Solimando, M. Pagliuca and A. Borzacchiello, *Polym. Chem.*, 2021, **12**, 6667–6687.
6 B. He, B. J. Burke, X. Zhang, R. Zhang and F. E. Regnier, *Anal. Chem.*, 2001, **73**, 1942–1947.
7 D. Erickson, D. Sinton and D. Li, *Lab Chip*, 2003, **3**, 141–149.
8 J. S. Hong, S. M. Stavis, S. H. Depaoli Lacerda, L. E. Locascio, S. R. Raghavan and M. Gaitan, *Langmuir*, 2010, **26**, 11581–11588.
9 R. Othman, G. T. Vladisavljević, N. L. Thomas and Z. K. Nagy, *Colloids Surf., B*, 2016, **141**, 187–195.
10 S. Lisina, W. Inam, M. Huhtala, F. Howaili, H. Zhang and J. M. Rosenholm, *Pharmaceutics*, 2023, **15**, 1–19.
11 D. Liu, H. Zhang, F. Fontana, J. T. Hirvonen and H. A. Santos, *Lab Chip*, 2017, **17**, 1856–1883.
12 D. Liu, H. Zhang, S. Cito, J. Fan, E. Mäkilä, J. Salonen, J. Hirvonen, T. M. Sikanen, D. A. Weitz and H. A. Santos, *Nano Lett.*, 2017, **17**, 606–614.
13 R. Karnik, F. Gu, P. Basto, C. Cannizzaro, L. Dean, W. Kyei-Manu, R. Langer and O. C. Farokhzad, *Nano Lett.*, 2008, **8**, 2906–2912.
14 A. Budhian, S. J. Siegel and K. I. Winey, *Int. J. Pharm.*, 2007, **336**, 367–375.
15 J. Y. Zhang, Z. G. Shen, J. Zhong, T. T. Hu, J. F. Chen, Z. Q. Ma and J. Yun, *Int. J. Pharm.*, 2006, **323**, 153–160.
16 S. Hornig, T. Heinze, C. R. Becer and U. S. Schubert, *J. Mater. Chem.*, 2009, **19**, 3838–3840.
17 B. K. Johnson and R. K. Prud'homme, *Phys. Rev. Lett.*, 2003, **91**, 118302.
18 S. Gimondi, H. Ferreira, R. L. Reis and N. M. Neves, *ACS Nano*, 2023, **17**, 14205–14228.
19 J. Guerrero, Y.-W. Chang, A. A. Fragkopoulos, A. Fernandez-Nieves, J. Guerrero, Y.-W. Chang, A. A. Fragkopoulos and A. Fernandez-Nieves, *Small*, 2020, **16**, 1904344.
20 J. M. Lim, A. Swami, L. M. Gilson, S. Chopra, S. Choi, J. Wu, R. Langer, R. Karnik and O. C. Farokhzad, *ACS Nano*, 2014, **8**, 6056–6065.
21 A. Jahn, W. N. Vreeland, M. Gaitan and L. E. Locascio, *J. Am. Chem. Soc.*, 2004, **126**, 2674–2675.
22 S. Laín, J. H. Lozano-Parada and J. Guzmán, *Appl. Sci.*, 2022, **12**, 3589.
23 R. Lindken, M. Rossi, S. Große and J. Westerweel, *Lab Chip*, 2009, **9**, 2551–2567.
24 L. Stern, A. Bakal, M. Tzur, M. Veinguer, N. Mazurski, N. Cohen and U. Levy, *Sensors*, 2014, **14**, 16799.
25 E. Yakhshi-Tafti, *Master's thesis*, University of Central Florida, 2009.
26 R. F. Laine, K. L. Tosheva, N. Gustafsson, R. D. M. Gray, P. Almada, D. Albrecht, G. T. Risa, F. Hurtig, A. C. Lindås, B. Baum, J. Mercer, C. Leterrier, P. M. Pereira, S. Culley and R. Henriques, *J. Phys. D: Appl. Phys.*, 2019, **52**(16), 163001.
27 *MSEGaussianFlow (Fiji Javadocs 0-SNAPSHOT API)*, **https://javadoc.scijava.org/Fiji/mpicbg/ij/plugin/MSEGaussianFlow.htmL**, (accessed 16 January 2024).
28 D. Ershov, M. S. Phan, J. W. Pylvänäinen, S. U. Rigaud, L. Le Blanc, A. Charles-Orszag, J. R. W. Conway, R. F. Laine, N. H. Roy, D. Bonazzi, G. Duménil, G. Jacquemet and J. Y. Tinevez, *Nat. Methods*, 2022, **19**, 829–832.
29 S. K. Filippov, R. Khusnutdinov, A. Murmiliuk, W. Inam, L. Y. Zakharova, H. Zhang and V. V. Khutoryanskiy, *Mater. Horiz.*, 2023, **10**, 5354–5370.
30 J. W. Swan and E. M. Furst, *J. Colloid Interface Sci.*, 2012, **388**, 92–94.
31 H. Ohshima, *J. Colloid Interface Sci.*, 2002, **255**, 202–207.
32 B. Suri, J. Tithof, R. O. Grigoriev and M. F. Schatz, *Phys. Rev. Lett.*, 2017, **118**, 114501.
33 M. V. Budyansky, M. Y. Uleysky and S. V. Prants, *J. Exp. Theor. Phys.*, 2004, **99**, 1018–1027.
34 A. Etminan, Y. S. Muzychka, K. Pope and B. Nyantekyi-Kwakye, *Meas. Sci. Technol.*, 2022, **33**, 092002.
35 E. Joshi, M. H. Thoma and M. Schwabe, *Phys. Rev. Res.*, 2024, **6**(1), L012013.
36 G. Haller, *Annu. Rev. Fluid Mech.*, 2018, **47**, 137–162.
37 J. Stetefeld, S. A. McKenna and T. R. Patel, *Biophys. Rev.*, 2016, **8**(4), 409–427.
38 V. K. LaMer and R. H. Dinegar, *J. Am. Chem. Soc.*, 1950, **72**, 4847–4854.
39 G. A. Voth, T. C. Saint, G. Dobler and J. P. Gollub, *Phys. Fluids*, 2003, **15**, 2560–2566.
40 Y. K. Suh and S. Kang, *Micromachines*, 2010, **1**, 82–111.